

The Signature of the Northern Galactic Center Region in Low-Velocity UV Absorption

CHRISTIAN SOTO,¹ TRISHA ASHLEY,¹ ANDREW J. FOX,^{2,3} AND RONGMON BORDOLOI⁴

¹*Space Telescope Science Institute, 3700 San Martin Drive, Baltimore, MD 21218*

²*AURA for ESA, Space Telescope Science Institute, 3700 San Martin Drive, Baltimore, MD 21218*

³*Department of Physics & Astronomy, Johns Hopkins University, 3400 N. Charles Street, Baltimore, MD 21218, USA*

⁴*Department of Physics, North Carolina State University, 421 Riddick Hall, Raleigh, NC 27695-8202*

ABSTRACT

The Galactic Center (GC) is surrounded by plasma lobes that extend up to ~ 14 kpc above and below the plane. Until now, UV absorption studies of these lobes have only focused on high-velocity components ($|v_{\text{LSR}}| > 100 \text{ km s}^{-1}$) because low- and intermediate-velocity (LIV) components ($|v_{\text{LSR}}| < 100 \text{ km s}^{-1}$) are blended with foreground interstellar medium. To overcome this difficulty, we present a differential experiment to compare the LIV absorption between different structures within the GC region, including the Fermi Bubbles (FBs; seen in γ -rays), the eROSITA Bubbles (eBs; seen in X-rays), and the Loop I North Polar Spur (LNPS) association, an X-ray and radio feature within the northern eB. We use far-UV spectra from Hubble Space Telescope to measure LIV Si IV absorption in 61 AGN sight lines, of which 21 pass through the FBs, 53 pass through the eBs, and 18 pass through the LNPS. We also compare our measurements to those in the literature from sight lines covering the disk-halo interface and CGM. We find that the FBs and eBs have enhancements in measured columns of 0.22-0.29 dex in log. We also remove the contribution of a modeled disk and CGM component from the measured Si IV columns and find that the northern eB still retains a Si IV enhancement of 0.62 dex in log. A similar enhancement is not seen in the southern eB. Since the LNPS model-subtracted residuals show an enhancement compared to the rest of the northern eB of 0.69 dex, the northern eB enhancement may be caused by the LNPS.

Keywords: Milky Way Galaxy — Milky Way evolution — Galactic Center

1. INTRODUCTION

The Fermi Bubbles (FBs) are two bipolar plasma lobes launched from the center of the Milky Way, reaching $\sim 55^\circ$ in Galactic latitude above and below the Galactic plane. Given their close proximity, we can use them as a laboratory to study the effect of nuclear feedback on the baryonic ecosystems of galaxies in greater detail than is possible in any other galaxy. Recent evidence suggests that the FBs likely formed ≈ 3 -6 Myr ago through an energetic outburst from Sagittarius A* (Zubovas et al. 2011; Guo & Mathews 2012; Yang et al. 2012; Bland-Hawthorn et al. 2013, 2019; Mou et al. 2014; Fox et al. 2020; Yang et al. 2022). For example, Bland-Hawthorn

et al. (2013, 2019) and Fox et al. (2020) find an excess in H α , C IV, and Si IV in the Magellanic Stream passing directly below the Galactic Center (GC). Models produced by Bland-Hawthorn et al. (2019) show that a Seyfert flare coming from Sagittarius A* 3.5 ± 1 Myr ago is necessary to produce those elevated present-day levels of H α in the Magellanic Stream. This timescale agrees with models that suggest the FBs formed via a jet or flare emanating from Sagittarius A* in the past 1-6 Myr (Zubovas et al. 2011; Guo & Mathews 2012; Yang et al. 2012). The timescale also agrees with the 6-9 Myr age of the UV-observed outflow modeled by Bordoloi et al. (2017). An alternative hypothesis for the growth of the FBs is nuclear star formation; although this would operate on a longer timescale of 30 – 100 Myr (Yusef-Zadeh et al. 2009; Lacki 2014; Crocker et al. 2015; Sarkar et al. 2015).

While the FBs are defined by the gamma-ray emitting regions of the nuclear outflow, counterparts at other wavelengths have also been detected in microwave, optical, and polarized radio emission (Bland-Hawthorn & Cohen 2003; Dobler & Finkbeiner 2008; Su et al. 2010; Dobler et al. 2010; Carretti et al. 2013; Ackermann et al. 2014; Krishnarao et al. 2020). Recently, an X-ray counterpart has also been discovered, the eROSITA Bubbles (eBs; Predehl et al. 2020). The eBs are similar in shape but extend further than the FBs, reaching $\pm 85^\circ$ in latitude or ~ 14 kpc in height. The northern eB also encompasses the multi-wavelength feature, called the Loop I and North Polar Spur (hereafter, LNPS) association (Hanbury Brown et al. 1960; Bower et al. 1968; Berkhuijsen et al. 1971; Haslam et al. 1982; Sofue & Reich 1979; Sun et al. 2013; Planck Collaboration et al. 2016; Predehl et al. 2020). The origin of the LNPS has long been debated. It is believed to trace either nearby supernova remnant projected in front of the GC ~ 100 – 200 pc away or a structure physically associated with the GC, or an overlapping projection of both a GC feature and nearby supernova remnant (see Lallement 2022, and references therein). Until recently, one strong argument against the LNPS being associated with the GC was that the LNPS had no southern Galactic counterpart. The discovery of a southern X-ray bubble (a.k.a. the southern eB) has reignited that debate (Predehl et al. 2020; Yang et al. 2022; Lallement 2022).

Discrete high-velocity clouds (HVCs) thought to be associated with the FBs have been detected in H I emission, CO emission, UV H_2 absorption, and UV-metal absorption towards AGN sight lines (McClure-Griffiths et al. 2013; Fox et al. 2015; Bordoloi et al. 2017; Savage et al. 2017; Di Teodoro et al. 2018; Di Teodoro et al. 2020; Karim et al. 2018; Lockman et al. 2020; Ashley et al. 2020, 2022; Cashman et al. 2021). The velocities of these clouds ($|v_{\text{LSR}}| > 100 \text{ km s}^{-1}$) are high enough to distinguish them from Milky Way disk gas at $|v_{\text{LSR}}| < 100 \text{ km s}^{-1}$. On the other hand, diffuse gas at *low* and *intermediate* velocities (LIV; $|v_{\text{LSR}}| < 100 \text{ km s}^{-1}$) have largely gone unexplored because they overlap with the Milky Way interstellar medium in velocity space, and are thus contaminated by foreground absorption.

This contamination issue can be overcome with a differential experiment in which absorption in FB sight lines is compared to absorption in nearby sight lines outside the bubbles. Since the plasma inside the FBs has a high ionization level, sight lines passing inside the bubbles are expected to show stronger high-ion absorption than sight lines passing outside. High ions are therefore an ideal tracer for this experiment. For example, Savage

et al. (2017) study a pair foreground-background stellar sightlines, which show enhancement of LIV Si IV and C IV absorption towards the southern FB, but they do not explore its significance. This effect was also seen by Wakker et al. (2012, hereafter W12) and Zheng et al. (2019, hereafter Z19), who measured the amount of LIV Si IV absorption towards 58 and 132 AGN sight lines, respectively, through the disk-halo interface and CGM, probing gas at temperatures of $\sim 10^4 - 10^5 \text{ K}$ (Gnat & Sternberg 2007). W12 and Z19 find an excess of 0.1–0.26 dex in LIV Si IV column densities towards the GC. Z19 suggest that this enhancement could be due to the FBs, but they do not explore it further.

In this paper, we present a differential survey of LIV Si IV absorption in sight lines that pass through various structures in the GC region, including the FBs, eBs, and LNPS, using UV spectra from the Hubble Space Telescope Cosmic Origins Spectrograph (HST/COS) and Space Telescope Imaging Spectrograph (HST/STIS). We chose to use Si IV doublet for this study because among the high-ion doublets in the COS bandpass, N V is often undetected and C IV is often saturated, while Si IV tends to yield a measurable column density (Fox et al. 2015; Bordoloi et al. 2017; Karim et al. 2018; Ashley et al. 2020). Additionally, using Si IV allows us to make direct comparisons of GC pointings to the extensive sample in Savage & Wakker (2009, hereafter S09), W12, and Z19 probing the rest of the disk-halo interface and CGM. In Section 2 we present our data-set and discuss our observations and data reduction. In Section 3 we present the results of our survey and discuss how our results compare to those in the literature. Our conclusions are then presented in Section 4.

2. OBSERVATIONS AND DATA REDUCTION

Our sample consists of 61 AGN sight lines with HST/COS and HST/STIS data drawn from the samples of Fox et al. (2015), Bordoloi et al. (2017), Karim et al. (2018), and Ashley et al. (2020); 21 pass through the FBs, 53 pass through the eBs, 18 pass through the LNPS association, and 8 pass through none of these GC features. For the sight lines passing through the FBs, the set also included targets that were listed in the literature as being on the “edge” of the bubble. Seven of the sight lines in our sample are close to the Magellanic System or have HVCs associated with the Magellanic Stream identified in their spectrum (see Table A1; Fox et al. 2014; Karim et al. 2018). As discussed in Section 3, the Magellanic Stream does not contribute an excess of LIV Si IV absorption to our measurements. Figure 1 shows the location of the sight lines relative to

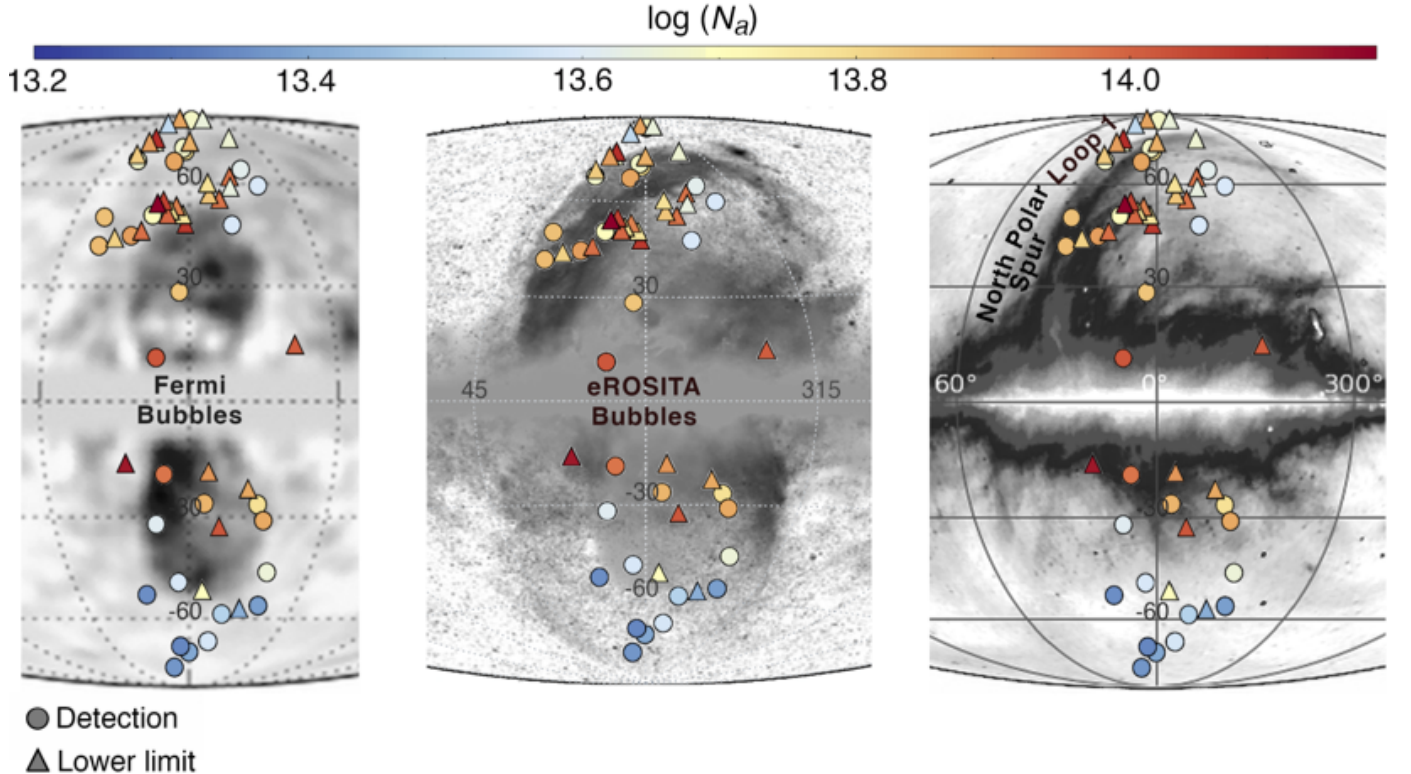


Figure 1. Maps showing the location of our sample sight lines and their $\log N_a(\text{Si IV})$ values (N_a in cm^{-2}) denoted by the colorscale. The circles are background quasars and the triangles indicate lower limits due to saturation. The background greyscales display the extent of the FBs, eBs, and LNPS association using the following adapted maps: (Left) a gamma-ray map from [Ackermann et al. \(2014\)](#) in Mollweide projection, (Middle) a combined gamma-ray and X-ray map from [Predehl et al. \(2020\)](#) in Hammer-Aitoff projection, and (Right) a 408 MHz emission map from [Haslam et al. \(1982\)](#) and reprocessed by [Remazeilles et al. \(2015\)](#) in Mollweide projection.

the FBs, eBs, and LNPS. In Table A1, we present basic information on each sight line.

Each sight line has a COS FUV G130M spectrum and one sight line (NGC5548) has STIS E140M spectrum. The COS data were initially calibrated with the `calcos` calibration pipeline. We then applied customized velocity alignment and co-addition steps described in [Wakker et al. \(2015\)](#), which align the Galactic absorption with H I emission.

We measure the apparent optical depths (AODs) and the apparent column densities (ACDs) of the LIV Si IV absorption using a custom Python package called `spectraAOD`¹ ([Magness et al. 2020](#)). AODs are used to analyze interstellar absorption lines; they represent the true optical depth with the addition of instrumental blurring ([Savage & Sembach 1991](#)). To make these measurements, `spectraAOD` first normalizes the spectrum using a straight line between two sections of user-determined continuum. Continuum ranges were chosen

for each ion visually, avoiding absorption features such as redshifted intergalactic absorbers and HVCs identified in previous work ([Fox et al. 2015](#); [Bordoloi et al. 2017](#); [Karim et al. 2018](#)). The velocity-dependent AOD, $\tau_a(v)$, is calculated as:

$$\tau_a(v) = -\ln[F_c(v)/F(v)], \quad (1)$$

where $F(v)$ is the flux of the absorption and $F_c(v)$ is the continuum flux. $\tau_a(v)$ is then used to find the apparent column density (N_a):

$$N_a = \int_{v_-}^{v_+} 3.768 \times 10^{14} \frac{\tau_a(v)}{f\lambda} dv \text{ cm}^{-2}, \quad (2)$$

where v_- and v_+ are the LSR velocity limits of the absorption, f is oscillator strength of the transition of interest ([Morton 2003](#)), and λ is the transition wavelength in Angstroms. For each sight line, we measure the AOD and ACD between -100 and 100 km s^{-1} for Si IV $\lambda\lambda 1393$ and 1402 . Figure 2 shows an example of `spectraAOD`'s graphical output, including the sight lines' spectra, continuum fits, and ACD measurements.

¹ <https://github.com/cmagness/spectraAOD>

`spectraOD` determines the noise using the standard deviation of the flux around the continuum. If the absorption reaches a minimum flux less than the noise anywhere within the line profile, then it is labeled as saturated. If the minimum flux is greater than the noise and the line is detected at 3σ significance (i.e., the equivalent width is at least three times the equivalent width error), then the absorption is labeled as detected. In all other cases, the absorption is labeled as not detected.

For lines that are unblended and unsaturated, the measured ACD from each member of the doublet should match within their respective measurement errors. However, different measurements may arise due to contamination from intergalactic absorption, continuum-fit errors, and/or unresolved saturation. The column-density measurements from each member of the doublet were considered to match if the following condition was met:

$$\frac{\log(N_{a2}) - \log(N_{a1})}{\sqrt{\sigma_2^2 + \sigma_1^2}} < 3 \quad (3)$$

where σ is the error on each logarithmic ACD measurement. If the value was >3 , then we inspected the spectrum to determine which doublet line was more reliable. For example, if an intergalactic absorber was found in the stronger line, then the weaker lines measurement was considered more reliable and was used.

In cases where both members of the Si IV doublet were detected and unsaturated, and the requirement of Equation 3 was met, we used the average of the two ACD measurements in our analysis. If both lines were saturated and visual inspection of the data did not reveal any issues with either line, then the weaker line was used to derive a lower limit on the ACD. If the stronger line was

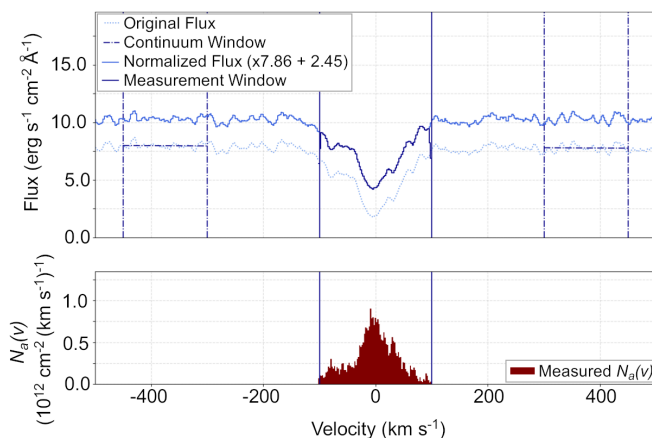


Figure 2. Example spectral plots from the `spectraOD` code for the sight line toward QSO ESO 141-G55, which passes through the southern FB. The top panel shows the Si IV 1393 line profile. The lower panel shows the ACD as a function of LSR velocity.

saturated and the weaker line was detected without apparent saturation, then we adopt the measurement from the weaker line. In this case, the weaker line was labeled as detected and unsaturated if the Equation 3 requirement was met, otherwise it was labeled as saturated to account for unresolved saturation.

3. RESULTS AND DISCUSSION

Of the 61 sight lines measured in our study, one sight line (SDSS J141038.40+230447.0) was unusable due to intergalactic absorption blending in both Si IV lines. Of the remaining 60 sight lines, the Si IV detection rate was 100%. For sight lines passing through the FBs, eBs, and LNPS 45%, 39%, and 60% respectively, are labeled as saturated.

3.1. Column-density dependence on Latitude and Longitude

S09, W12, and Z19 measured the LIV Si IV absorption through the MW disk and CGM with 31, 58, and 132 extragalactic sight lines covering the entire sky. W12 and Z19 found that their LIV Si IV column density measurements increase slightly by 0.1–0.26 dex in directions towards the GC regions, and Z19 suggest this enhancement could be due to the FBs.

To understand how the Si IV measurements in our GC sample compare to Si IV in the rest of the disk-halo interface and CGM, we combine the S09, W12, and Z19 results with our own in Figure 3 where we plot $\log(N_a \sin|b|)$ vs. Galactic latitude and longitude. $\log(N_a \sin|b|)$ measures the z-axis-projected column densities, where the z-axis perpendicular to the Galactic plane, and is designed to correct for disk projection effects. In a simple exponential disk model, $\log(N_a \sin|b|)$ is a constant and thus becomes independent of Galactic latitude (Savage et al. 1990; Savage & Wakker 2009; Zheng et al. 2019).

Of the 31, 58, and 132 sight lines from the S09, W12, and Z19 samples, 3, 3, and 23 sight lines overlap with our sample, respectively. We compare the $\log(N_a)$ measurements for the 23 overlapping Z19 sight lines and find they agree within the errors. We note that W12 and Z19 use a stricter 1σ criteria for defining matching doublet column density measurements, whereas our threshold is 3σ . We also note that W12 integrates over a variable velocity range that is determined by the visual identification of the thick disk component.

In the top panel of Figure 3 we plot $\log(N_a \sin|b|)$ vs. Galactic longitude for our sample and all three comparison samples. In the figure, the $\log(N_a \sin|b|)$ Si IV values in the GC region stand out clearly against the

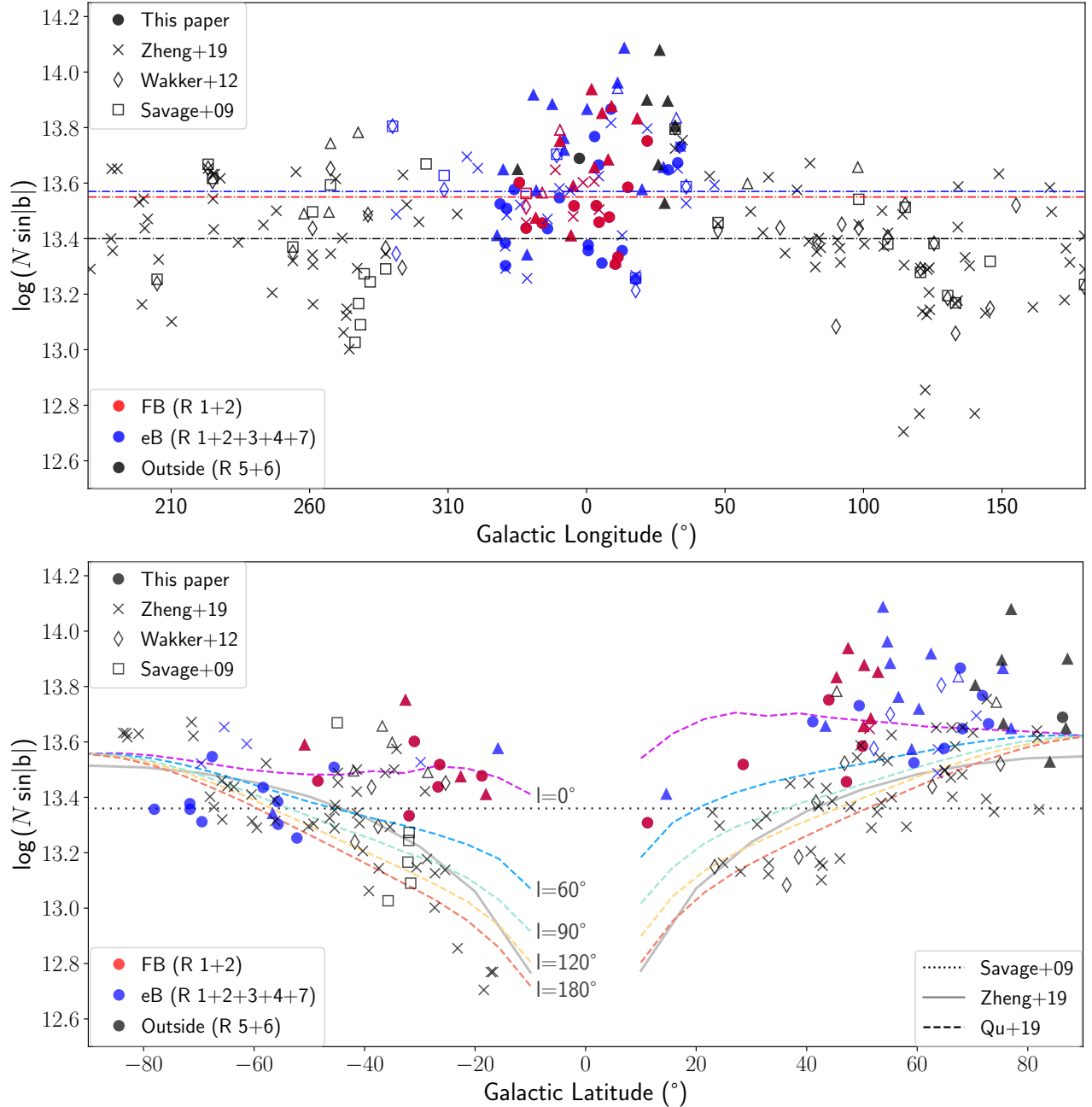


Figure 3. Si IV columns projected onto the z -axis, $\log(N_a \sin|b|)$, vs. Galactic longitude (top) and Galactic latitude (bottom) for our sample (filled circles and triangles), the Z19 sample (crosses and empty triangles), the W12 sample (diamonds and empty triangles), and the S09 sample (squares and empty triangles). Red symbols depict sight lines inside the FBs, blue symbols depict sight lines inside the eBs, and black symbols depict sight lines outside of both bubbles. Triangles represent saturated values. In the top panel, the black, red, and blue horizontal lines are the mean unsaturated values for lines outside of the bubbles (13.41), inside the FBs (13.55), and inside the eBs (13.58) for all samples excluding overlapping sight lines. In the bottom panel the black horizontal dotted line represents the flat-slab model predicted value (13.36; S09), the grey solid line represents the predicted values from the Z19 model, and the dashed colored lines represent the Qu & Bregman (2019) models for a variety of longitudes.

rest of the Galactic halo, with GC sight lines having $\log(N_a \sin|b|) \gtrsim 13.8$.

To see this effect in Galactic latitude, we plot $\log(N_a \sin|b|)$ vs. b . Figure 3 shows higher Si IV column

densities at positive latitudes, demonstrating an asymmetry between the northern and southern hemispheres. The northern enhancement in $\log(N_a \sin|b|)$ appears to occur within both the FB and eB latitude boundaries.

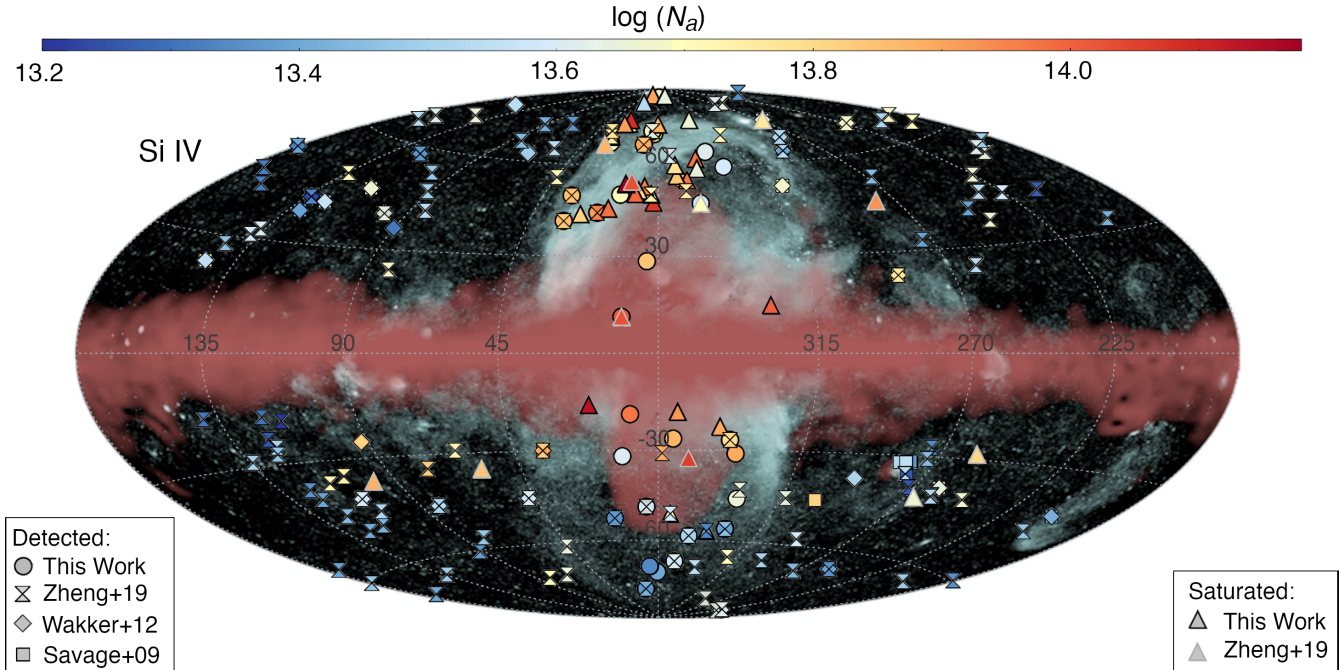


Figure 4. Measured LIV $\log N_a(\text{Si IV})$ values (N in cm^{-2}) from this paper, S09, W12, and Z19 projected onto the combined gamma-ray (red) and X-ray (cyan) map of the FBs and eBs adapted from Predehl et al. (2020). The LNPS association appears in this image as the strong X-ray emission in the top-left of the northern eB.

In the bottom panel of Figure 3, we plot the Si IV column density predictions of three models of the disk-halo interface. First, we plot the S09 model which assumes that the disk column density decreases exponentially with a fixed scale height (plane-parallel slab model). Second, we plot the Z19 two-component model which adds a latitude-dependent CGM component to the plane-parallel slab model. Third we plot the Qu & Bregman (2019) model which accounts for a two-dimensional radial distribution of the disk-halo interface with a latitude-dependent CGM. None of these models appear to account for the high columns in the northern sky. Qu & Bregman (2019) and Qu et al. (2020) also notice a north-south asymmetry in Si IV columns and attempt to account for it by artificially increasing the northern sight lines absorption, increasing their model limits from $\log(N_a \sin|b|) \lesssim 13.55$ to $\lesssim 13.75$. Even with this increase in the modeled northern $\log(N_a \sin|b|)$ values, Figure 3 indicates that the GC northern enhancement in Si IV measured columns cannot be explained from the shape of the disk-halo interface.

To understand exactly where these enhancements arise, we plot the measured $\log(N_a)$ values of all samples on a map of the full sky X-ray and gamma-ray emission from Predehl et al. (2020) in Figure 4. This figure shows both the FBs and eBs. In Figure 4, the eBs and FBs visually appear to have much higher Si IV than the rest of

the sky. We discuss the statistics of potential enhancements in Si IV absorption below in detail in Section 3.2.

3.2. Statistical Analysis of Spatially-Selected Regions

To quantitatively assess the enhancement in Si IV absorption towards the GC, we merge our sample with the S09, W12, and Z19 samples and then divide it into eight spatially-selected comparison sets, as shown in Tables 1 and 2 and Figure 5. For the overlapping sight lines between our sample and comparison samples, we use our sample’s measurements. We then choose which of the overlapping sight lines in the comparison samples to use based on the following priority: (1) Z19, (2) W12, and (3) S09. The only exception to this are the sight lines 3C273 and PKS0405-123, which appear in the Z19 as having unreliable Si IV column measurements due to a $\lambda 1393$ measurement that is abnormally stronger than the $\lambda 1402$ measurement. For those sight lines, we use the W12 value, who identified a reliable measurement when Lyman α interference and specific velocity ranges were taken into account.

For our statistical analysis, we analyze two sets of combined data:

- The Si IV column density measurements: analysis of the observed columns (see Figure 4) allows us to directly look for GC features that stand out compared to other measurements in a model-independent manner, without making assumptions

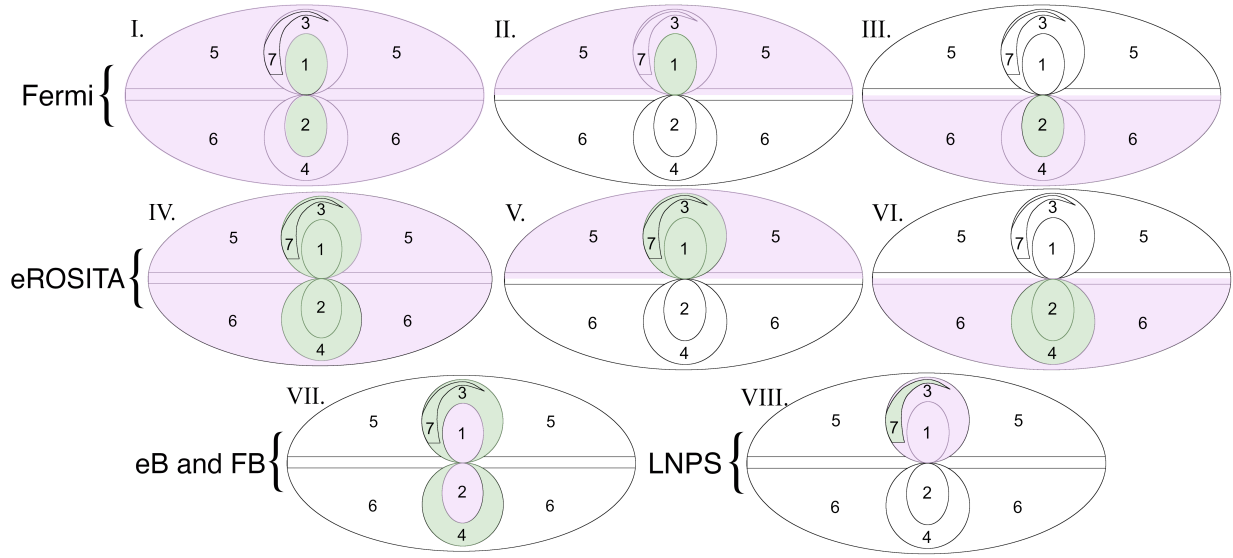


Figure 5. Maps of the sky regions explored in this study: FBs (1 and 2), eBs (3 and 4), sky regions exterior to the bubbles (5 and 6), and LNPS (7). The numbers and shading label the spatially-selected comparison groups referenced in Tables 1 and 2.

Table 1. Statistical analysis of N_a (Si IV) values combined from this work, S09, W12, and Z19

| | | Spatially-Selected Comparison Groups ^a | Count Unsaturated ^b | Count Saturated ^c | Basic Statistics | | Statistical Test ^f | | |
|---------|----------------------|--|-----------------------------------|---------------------------------|-------------------------------------|--------------------------------|-------------------------------|---------------------------------------|-------------------|
| | | | | | $\log(\overline{N}_a)$ ^d | Standard Error ^e | χ^2 | p -value | Test ^g |
| Fermi | I. | Inside FBs (R 1+2) | 12 | 10 | 13.93 | 0.03 | 20.1 | 7×10^{-6} | P |
| | | Outside FBs (R 3+4+5+6+7) | 137 | 28 | 13.71 | 0.03 | | | |
| | II. | Inside FB: North (R 1) | 6 | 6 | 13.94 | 0.04 | 8.5 | 0.004 | P |
| | | Outside FB: North (R 3+5+7) | 66 | 22 | 13.79 | 0.04 | | | |
| | III. | Inside FB: South (R 2) | 6 | 4 | 13.89 | 0.04 | 14 | 2×10^{-4} | L |
| | | Outside FB: South (R 4+6) | 71 | 6 | 13.60 | 0.03 | | | |
| eROSITA | IV. | Inside eBs (R 1+2+3+4+7) | 39 | 25 | 13.91 | 0.03 | 39 | 4×10^{-10} | L |
| | | Outside eBs (R 5+6) | 110 | 13 | 13.62 | 0.03 | | | |
| | V. | Inside eB: North (R 1+3+7) | 19 | 19 | 13.96 | 0.04 | 32.9 | 1×10^{-8} | P |
| | | Outside eB: North (R 5) | 53 | 9 | 13.66 | 0.04 | | | |
| | VI. | Inside eB: South (R 2+4) | 20 | 6 | 13.78 | 0.06 | 8.6 | 0.003 | L |
| | | Outside eB: South (R 6) | 57 | 4 | 13.56 | 0.02 | | | |
| VII. | Inside eBs (R 3+4+7) | 27 | 15 | 13.86 | 0.05 | 5.7 | 0.02 | P | |
| | Inside FBs (R 1+2) | 12 | 10 | 13.93 | 0.03 | | | | |
| LNPS | VIII. | Inside LNPS (R 7) | 8 | 12 | 14.01 | 0.05 | 1.7 | 0.2 | L |
| | | Inside eB: North (R 1+3) | 11 | 7 | 13.87 | 0.05 | | | |

^aSpatially-selected groups are compared two at a time with the comparison set bracketed by horizontal lines. The region (R) covered by these different group is denoted by a number shown in Figure 5.

^bThe number of unsaturated sight lines.

^cThe number of saturated sight lines.

^dThe log of the restricted mean apparent column density. The restricted mean is calculated using an upper limit set to the maximum column density in each spatially selected group.

^eThe standard error on the log restricted mean.

^fComparison sets with statistics in bold are likely drawn from separate populations.

^gSurvival test used in the `survdif` function: P = Peto-Peto test and L = Log-rank test.

about the shape of the disk. While statistically

comparing the GC data to the entirety of the rest

Table 2. Statistical analysis of disk-model-subtracted $N_a(\text{Si IV})$ values combined from this work, S09, W12, and Z19

| | | Spatially-Selected Comparison Groups ^a | Count Unsaturated ^b | Count Saturated ^c | Basic Statistics | | Statistical Test ^f | | |
|--------------------|-------|--|-----------------------------------|---------------------------------|---|--------------------------------|-------------------------------|--------------|-------------------|
| | | | | | $\log(\overline{N_{a,R}})$ ^d | Standard Error ^e | χ^2 | p-value | Test ^g |
| Fermi | I. | Inside FBs (R 1+2) | 12 | 10 | 13.18 | 0.22 | 0.6 | 0.4 | P |
| | | Outside FBs (R 3+4+5+6+7) | 137 | 28 | 13.10 | 0.09 | | | |
| | II. | Inside FB: North (R 1) | 6 | 6 | 13.16 | 0.37 | 0.1 | 0.7 | P |
| | | Outside FB: North (R 3+5+7) | 66 | 22 | 13.24 | 0.10 | | | |
| | III. | Inside FB: South (R 2) | 6 | 4 | 13.18 | 0.22 | 1.2 | 0.3 | L |
| | | Outside FB: South (R 4+6) | 71 | 6 | 12.76 | 0.13 | | | |
| eROSITA | IV. | Inside eBs (R 1+2+3+4+7) | 39 | 25 | 13.42 | 0.10 | 2.9 | 0.09 | P |
| | | Outside eBs (R 5+6) | 110 | 13 | 12.91 | 0.11 | | | |
| | V. | Inside eB: North (R 1+3+7) | 19 | 19 | 13.56 | 0.11 | 10.5 | 0.001 | L |
| | | Outside eB: North (R 5) | 53 | 9 | 12.93 | 0.17 | | | |
| | VI. | Inside eB: South (R 2+4) | 20 | 6 | 12.79 | 0.29 | 0.0 | 1 | L |
| | | Outside eB: South (R 6) | 57 | 4 | 12.83 | 0.12 | | | |
| | VII. | Inside eBs (R 3+4+7) | 27 | 15 | 13.38 | 0.12 | 0.2 | 0.6 | L |
| Inside FBs (R 1+2) | | 12 | 10 | 13.18 | 0.22 | | | | |
| LNPS | VIII. | Inside LNPS (R 7) | 8 | 12 | 13.67 | 0.10 | 5.1 | 0.02 | P |
| | | Inside eB: North (R 1+3) | 11 | 7 | 12.98 | 0.39 | | | |

^aSee Table 1 for table notes. Here the column densities have been disk-subtracted using the model of Qu & Bregman (2019).

of disk-halo interface and CGM does not account for Galactic structure, our goal in this section is simply to measure the significance of the GC enhancement against the rest of the sky. This global approach is necessary because splitting the sky into different longitude or latitude bands for statistical tests provides samples that are too small to obtain statistically significant results.

- The disk-CGM model-subtracted Si IV residuals: we analyze the residuals formed by subtracting the Qu & Bregman (2019) two-dimensional disk-CGM Si IV model from the Si IV column measurements (see the top panel of Figure 6). The Qu & Bregman (2019) model contains a radial- and height-dependent disk component and a constant CGM component, with Si IV column densities determined by minimized χ^2 models using AGN and stellar sight line measurements. For each of our sight lines we determine the model column at that sky position and subtract it from the observed column to obtain a residual. This model-dependent analysis allows us to remove effects from the Galactic disk component on the column densities. These effects are particularly strong at low latitudes where sight lines pass through more of the ISM.

Throughout the remainder of the paper, we will refer to these two datasets as the column density measurements and model-subtracted residuals, respectively.

Since a significant portion of the sight lines towards the GC are lower limits, we use survival analysis to account for censored data. Specifically, we use the `survival` package function, `survfit` in the language R to calculate each spatial group’s restricted mean and its associated standard error (see Tables 1 and 2 for the column-density measurements and model-subtracted residual analysis, respectively; R Core Team 2023; Therneau & Grambsch 2000; Therneau 2023). `survfit` uses the Kaplan-Meier method to create a survival curve for the data and then estimates the mean value using a range of acceptable columns (a.k.a. the restricted mean, $\overline{N_{a,R}}$; Miller 1981). For this analysis, we calculated the restricted mean by setting the maximum allowed column density in each spatially-selected group to the maximum column density of that specific spatial group.

Additionally, we use `survdif` function to determine if the two groups being compared are likely drawn from separate populations using either the log-rank or Peto-Peto test. The log-rank test gives equal weighting to all column density measurements and assumes proportional hazards (Mantel 1966; Cox 1972). The Peto-Peto

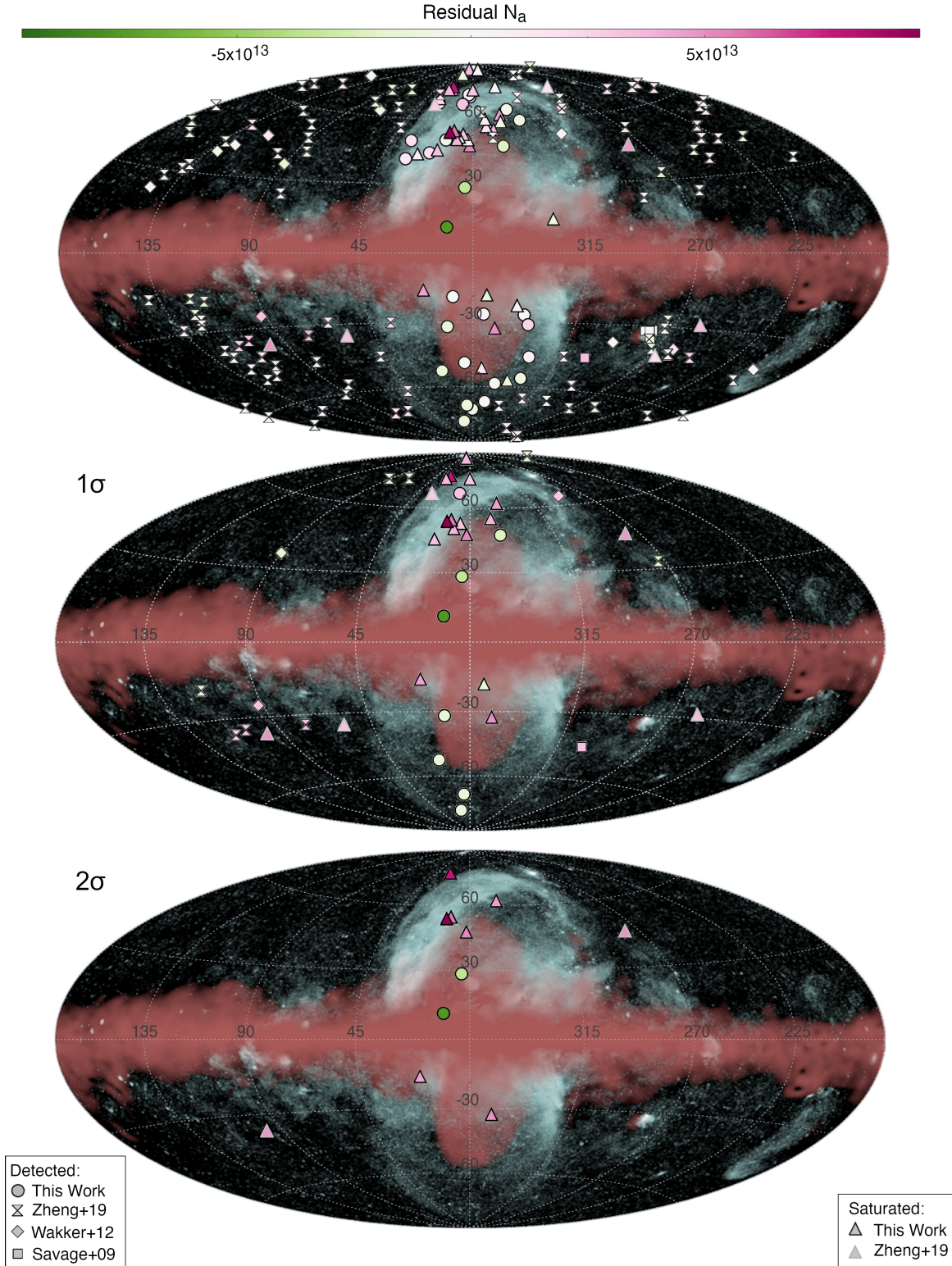


Figure 6. Column-density residuals after the subtraction of the Qu & Bregman (2019) disk model in the combined samples of this paper, S09, W12, and Z19. Enhancements and deficits in densities are denoted in green and pink, respectively. The top panel represents all sight lines, the middle and bottom panels represents all sightlines with residuals 1σ and 2σ away from the mean, respectively.

test gives a larger weight to low column densities and is a more appropriate test for when the assumption proportional hazards is violated (Gehan 1965; Peto & Peto 1972). We decide which test to use by running the `cox.zph` function for each set of spatially selected comparison groups, a function that tests whether proportional hazards can be assumed (Grambsch & Therneau 1994; Therneau & Grambsch 2000). In the results of both the log-rank or Peto-Peto tests, the χ^2 value is an indication of how different the two survival curves are from what would be expected if they were drawn from the same population. The results also provide p -values which need to be < 0.05 (95% confidence) in order to reject the null hypothesis that the two spatially selected groups are drawn from the same population. For examples of the survival curves used in this analysis, see Appendix B.

All statistical tests were performed using the linear (not logarithmic) form of N_a . Survival analysis requires the values being evaluated to be positive, but the model-subtracted analysis results in both positive and negative residuals. As a solution, we found the minimum column residual in each pair of spatially compared groups and added the minimum residual to all residuals in both samples prior to running the statistical tests. This process ensures the survival analysis is conducted only on positive numbers and that the two compared groups are shifted by the same amount. After the tests, we then shift all restricted mean values by subtracting their respective minimum residual, accounting for our previous offset. The results of these tests are shown in Tables 1 and 2, and spatially selected groups that are likely drawn from separate populations are highlighted in bold.

3.2.1. Sight Lines Inside vs. Outside the FBs

Survival analysis tests indicate different populations for *measured columns* in all spatially-compared groups associated with the FBs ($p \leq 0.004$). The sight lines passing through the FBs have a Si IV $\log(\overline{N_a})$ value 0.22 ± 0.04 dex higher than the sight lines passing outside (Table 1; Figure 5: regions 1+2 vs. 3+4+5+6+7). This holds true in the northern Galactic hemisphere with a 0.15 ± 0.06 dex difference (Figure 5: regions 1 vs. 3+5+7) and the southern Galactic hemisphere with a 0.39 ± 0.05 dex difference (Figure 5: regions 2 vs. 4+6; see Table 1).

The survival analysis tests for the *model-subtracted residual* absorption do not show a difference in the populations for the Fermi Bubble (FB) spatially-selected comparison groups. Therefore, the location of the FB sight lines relative to the disk may be playing a large role in the excess of Si IV columns in FB sight lines.

3.2.2. Sight Lines Passing Through vs. Outside the eBs

The survival tests for the *measured columns* indicate a difference in the population for all sight lines inside vs. outside the eBs (Figure 5: regions 1+2+3+4+7 vs. 5+6; $p = 4 \times 10^{-10}$) and eB sight lines vs. non-eB sight lines in the southern Galactic hemisphere (regions 2+4 vs. 6; $p = 0.003$). On the other hand, their *model-subtracted residual* absorption do not show a difference in the populations of all and southern eB sight lines to non-eB sight lines. This could indicate that the disk is contributing to the differences in the populations.

For sight lines passing through the *northern* eB (Figure 5: regions 1+3+7) both the measured N_a and residual $N_{a,R}$ values have significantly different populations than northern directions outside the eB (Figure 5: region 5), with p -values of 1×10^{-8} and 1×10^{-3} and differences of 0.30 ± 0.06 and 0.63 ± 0.20 dex, respectively.

Between the measured and model-subtracted column density analysis, only the statistical tests for inside vs. outside the northern eROSITA Bubble show a difference in population in both Tables 1 and 2. This result indicates that there is strong absorption enhancement in the northern eB. The northern eB also has a model-subtracted $\log(\overline{N_{a,R}})$ value 0.77 ± 0.39 dex higher than the southern eB (0.18 ± 0.07 dex higher in the measured $\log(\overline{N_a})$; see Tables 1 and 2). We ran additional statistical tests for the eB north vs. south and found that the measured and model subtracted columns are likely drawn from different populations ($\chi^2 = 11.1$ and 6.1 , $p = 0.0009$ and 0.01 , respectively), further highlighting the asymmetry in the northern and southern GC features seen in Figure 3.

3.2.3. Sight Lines Passing Through the FBs vs. eBs

We continue to explore relationships of these different spatial regions by looking at sight lines that pass through the FBs (Figure 5: regions 1+2) and sight lines passing through the eBs, but *not* the FBs (Figure 5: regions 3+4+7). Only the measured columns indicate that the populations are different ($p = 0.02$). However, this difference may depend on the location of the sight lines with respect to the disk as we do not see a population difference in the model-subtracted survival test.

3.2.4. LNPS and Northern eB Sight Lines

Strong Si IV absorption is detected along the sight lines associated with the northern eB and LNPS association (Figure 4). To explore the specific role of the LNPS in the northern eB's LIV Si IV enhancement, we separate out the sight lines passing through emission associated with LNPS.

In Figure 7 we have plotted all of the sight lines selected as passing through the LNPS association in opaque symbols. These sight lines were selected based on

the 408 MHz continuum emission (Haslam et al. 1982; Remazeilles et al. 2015) and the Spektr-RG–eROSITA all-sky survey (Predehl et al. 2020). We select the regions encompassed by LNPS based on definitions in the literature, such as Sofue (2015), Planck Collaboration et al. (2016), LaRocca et al. (2020), and references therein. As such, we select this sample based on LNPS’s multi-wavelength appearance so that we include all sight lines that may pass through the LNPS association. We chose not to include the faint southern structures that are at times associated with Loop I (Loop Is and the southern extension of Loop XII) because their connection with the northern LNPS association is not clear; it is possible that this structure is related to the southern eROSITA bubble or separate supernovae remnants (Berkhuijsen et al. 1971; Sofue & Reich 1979; Planck Collaboration et al. 2016; Predehl et al. 2020; Panopoulou et al. 2021; Lallement 2022).

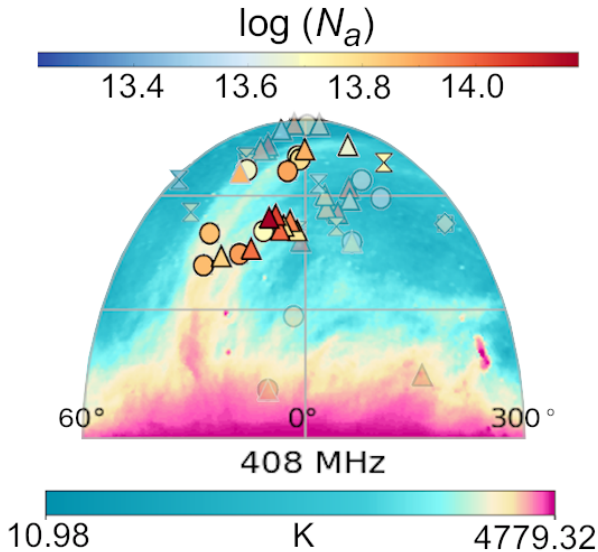


Figure 7. Illustration of the location of the LNPS. 408 MHz continuum emission from Haslam et al. (1982) and reprocessed by Remazeilles et al. (2015) is shown in the color scale. Overplotted are the sight lines from this study, S09, W12, and Z19, with the same labeling scheme as Figure 4. Sight lines that are considered to pass through the LNPS association for this study are opaque, while sight lines not included in the LNPS statistics for this study are transparent.

We compare the LNPS to the rest of the northern eB and do not find that the *measured-column* populations are different from one another (Figure 5: regions 7 vs. 1+3). However, the survival test for the *model-subtracted* analysis does show a difference in the populations with a p -value of 0.02 and $\chi^2 = 5.1$. The LNPS has a model-

subtracted $\log(\overline{N_{a,R}})$ enhancement of 0.69 ± 0.40 dex compared to the rest of the northern eB (see Table 2).

3.3. Si IV Enhancements towards the GC

To better understand these enhancements in Si IV, we have plotted sight lines in the model-subtracted analysis with residuals greater than 1σ and 2σ away from the mean in the middle and bottom panels of Figure 6, respectively. For this simple visual, we calculate the mean and standard deviation assuming that all values (including saturated values) are measurements, giving us a mean of $6.0 \times 10^{12} \text{ cm}^{-2}$ and a standard deviation of $1.9 \times 10^{13} \text{ cm}^{-2}$. From these plots we see several 1σ enhancements (positive residuals) in sight lines near latitudes of -30° and the strongest outliers detected near longitudes of 0° with both enhancements and deficits (negative residuals) in sight lines. The 1σ enhancements near the -30° latitude line visually appear parallel to the disk and may reflect the inherent patchiness of the CGM and/or an underestimation of the disk contribution in the model at this latitude. The Si IV enhancements and deficits in sight lines close to the 0° longitude line are so strong that they persist in the 2σ outliers plot on the bottom of panel in Figure 6. These 2σ enhancements and deficits near 0° longitude could be an indication that the model does not reproduce accurate columns at low longitudes.

To check how accurately the model reproduces the column densities at low longitudes, we use the Si IV measurement from the sight line toward HD 167402, a star at the distance of 7.0 ± 1.7 kpc with $l, b = 2.26^\circ, -6.39^\circ$ that is towards the GC, but does not pass through GC features (see Savage et al. 2017). This sight line has a measured LIV $\log N(\text{Si IV})$ of 13.65 while the model predicts a log column of 13.90, a difference of 0.25 dex ($\sim 3.5 \times 10^{13} \text{ cm}^{-2}$). This indicates that the model appears to be *overestimating* the columns at low longitudes. If so, then the enhancements in the northern sight lines that are close to 0° longitude may be *even higher* than indicated in Figure 6. This would strengthen the conclusion from the statistical tests that there is a strong Si IV enhancement towards the northern eB and LNPS.

If this excess absorption were associated with the Fermi or eBs alone, then we would expect these sight lines to be spread throughout both the northern and southern GC pointings. While a couple of enhanced southern GC sight lines are in the 2σ outlier plot, these two sight lines also fall close to the -30° latitude line, which shows a general enhancement, possibly contributing to the enhancement in these two sight lines’ residuals. Figure 6, combined with the statistical results in Tables 1 and 2, indicate that the northern eB has an en-

hancement of Si IV. Since the LNPS occurs in the northern Galactic hemisphere but not the southern Galactic hemisphere, and most of the excess absorption is contained in the north, the excess absorption may be associated with the LNPS. Additionally, an enhancement towards the LNPS in FUV C IV emission was found by Park et al. (2007), supporting an enhancement in high ions towards LNPS. The enhancement in the Si IV LIV absorption suggests that the eB and LNPS can be detected and characterized through excess Si IV absorption.

4. CONCLUSIONS

We have used archival HST/COS spectra to measure the apparent column densities of LIV Si IV absorption along 61 AGN sight lines in the GC region (within $\pm 30^\circ$ in longitude of the GC). We have used these measurements to look for low-velocity signatures of high-ion absorption in three structures in the Galactic Center region: the FBs, eBs, and LNPS association. Using statistical tests that account for censored data, we look for signatures of these features in the measured Si IV column densities and in the residuals after the disk-CGM components are subtracted off, using the models of Qu & Bregman (2019). Our results are as follows:

1. **Fermi Bubbles:** We find larger measured LIV Si IV column densities in sight lines passing through the FBs than in sight lines passing outside, with a mean enhancement of 0.22 dex. However, when we subtract the disk-CGM components, a survival analysis test finds that the columns inside and outside the FBs are not drawn from different populations. This may indicate that the disk (foreground) Si IV absorption is creating the differential between the two regions.
2. **eROSITA Bubbles:** Survival tests between directions through the northern eB and the rest of the northern hemisphere reveal a significant difference in the distribution of LIV Si IV column densities. This is true for both the measured and model-subtracted columns. The northern eB has Si IV columns 0.30 and 0.63 dex higher than the rest of the northern hemisphere in measured and model-subtracted columns, respectively.
3. **Northern enhancement:** The northern eB has a significantly higher mean Si IV column than the southern eB for both the measured and model-subtracted analysis (0.18 and 0.77 dex higher, respectively), revealing a strong asymmetry between the northern and southern bubbles. This can be

seen in plots of the Si IV residuals (observed – model column densities), which show that Si IV enhancements are clustered in the northern eB (Figure 6).

4. **Loop I North Polar Spur (LNPS):** If the Si IV enhancement were primarily related to the eBs, then it would be expected in both hemispheres. The lack of a southern counterpart to this enhancement suggests that the LNPS (which lies in the north) may be the underlying source of the excess Si IV LIV absorption. Statistical tests indicate an enhancement of 0.69 dex in the LNPS when compared to the rest of the northern eB. The LNPS enhancement is also supported by C IV emission measurements by Park et al. (2007).

The results in this paper indicate a new method for detecting the northern eB and possibly the LNPS. The asymmetries detected in the Si IV absorption reflect those seen in the X-ray, gamma-ray, and radio emission of the GC features. The source of the GC north-south brightness asymmetry and east-west asymmetry caused by the LNPS, is still a subject of debate. Some suggested sources include: variations in halo gas densities (Sarkar 2018; Sofue 2019), overlapping emission from a GC plasma bubble and a nearby supernova remnant (Predehl et al. 2020), the outflow encountering the 3 kpc molecular ring in the GC (Sofue & Kataoka 2021), and CGM winds impacting the outflow (Sofue 2019; Mou et al. 2023). The Si IV measurements presented in this paper provide useful constraints for future models that attempt to understand the origins of the asymmetries in GC features.

5. ACKNOWLEDGEMENTS

We would like to thank the anonymous referee for their helpful comments. We would like to thank Zhi-jie Qu for providing us the disk-halo model from Qu & Bregman (2019). We gratefully acknowledge support from the NASA Astrophysics Data Analysis Program (ADAP) under grant 80NSSC20K0435, *3D Structure of the ISM toward the Galactic Center* and from the STScI Director’s Discretionary Fund. The HST COS data presented in this paper were obtained from the Mikulski Archive for Space Telescopes (MAST) at the Space Telescope Science Institute. The specific observations analyzed for the sample in this paper can be accessed via MAST: [10.17909/jeph-7j87](https://archive.stsci.edu/missions/hst/cos/10.17909/jeph-7j87).

REFERENCES

- Ackermann, M., Albert, A., Atwood, W. B., et al. 2014, *The Astrophysical Journal*, 793, 64, doi: [10.1088/0004-637x/793/1/64](https://doi.org/10.1088/0004-637x/793/1/64)
- Ashley, T., Fox, A. J., Cashman, F. H., et al. 2022, *Nature Astronomy*, doi: [10.1038/s41550-022-01720-0](https://doi.org/10.1038/s41550-022-01720-0)
- Ashley, T., Fox, A. J., Jenkins, E. B., et al. 2020, *The Astrophysical Journal*, 898, 128, doi: [10.3847/1538-4357/ab9ff8](https://doi.org/10.3847/1538-4357/ab9ff8)
- Berkhuijsen, E. M., Haslam, C. G. T., & Salter, C. J. 1971, *A&A*, 14, 252
- Bland-Hawthorn, J., & Cohen, M. 2003, *The Astrophysical Journal*, 582, 246, doi: [10.1086/344573](https://doi.org/10.1086/344573)
- Bland-Hawthorn, J., Maloney, P. R., Sutherland, R. S., & Madsen, G. J. 2013, *The Astrophysical Journal*, 778, 58, doi: [10.1088/0004-637x/778/1/58](https://doi.org/10.1088/0004-637x/778/1/58)
- Bland-Hawthorn, J., Maloney, P. R., Sutherland, R., et al. 2019, *The Astrophysical Journal*, 886, 45, doi: [10.3847/1538-4357/ab44c8](https://doi.org/10.3847/1538-4357/ab44c8)
- Bordoloi, R., Fox, A. J., Lockman, F. J., et al. 2017, *The Astrophysical Journal*, 834, 191, doi: [10.3847/1538-4357/834/2/191](https://doi.org/10.3847/1538-4357/834/2/191)
- Bower, C. S., Field, G. B., & Mack, J. E. 1968, *Nature*, 217, 32, doi: [10.1038/217032a0](https://doi.org/10.1038/217032a0)
- Carretti, E., Crocker, R. M., Staveley-Smith, L., et al. 2013, *Nature*, 493, 66 EP . <https://doi.org/10.1038/Natureure11734>
- Cashman, F. H., Fox, A. J., Savage, B. D., et al. 2021, *The Astrophysical Journal Letters*, 923, L11, doi: [10.3847/2041-8213/ac3cbc](https://doi.org/10.3847/2041-8213/ac3cbc)
- Cox, D. R. 1972, *Journal of the Royal Statistical Society: Series B (Methodological)*, 34, 187, doi: <https://doi.org/10.1111/j.2517-6161.1972.tb00899.x>
- Crocker, R. M., Bicknell, G. V., Taylor, A. M., & Carretti, E. 2015, *The Astrophysical Journal*, 808, 107, doi: [10.1088/0004-637x/808/2/107](https://doi.org/10.1088/0004-637x/808/2/107)
- Di Teodoro, E. M., McClure-Griffiths, N. M., Lockman, F. J., & Armillotta, L. 2020, *Nature*, 584, 364, doi: [10.1038/s41586-020-2595-z](https://doi.org/10.1038/s41586-020-2595-z)
- Di Teodoro, E. M., McClure-Griffiths, N. M., Lockman, F. J., et al. 2018, *The Astrophysical Journal*, 855, 33, doi: [10.3847/1538-4357/aaad6a](https://doi.org/10.3847/1538-4357/aaad6a)
- Dobler, G., & Finkbeiner, D. P. 2008, *The Astrophysical Journal*, 680, 1222, doi: [10.1086/587862](https://doi.org/10.1086/587862)
- Dobler, G., Finkbeiner, D. P., Cholis, I., Slatyer, T., & Weiner, N. 2010, *The Astrophysical Journal*, 717, 825, doi: [10.1088/0004-637x/717/2/825](https://doi.org/10.1088/0004-637x/717/2/825)
- Fox, A. J., Frazer, E. M., Bland-Hawthorn, J., et al. 2020, *The Astrophysical Journal*, 897, 23, doi: [10.3847/1538-4357/ab92a3](https://doi.org/10.3847/1538-4357/ab92a3)
- Fox, A. J., Wakker, B. P., Barger, K. A., et al. 2014, *The Astrophysical Journal*, 787, 147, doi: [10.1088/0004-637x/787/2/147](https://doi.org/10.1088/0004-637x/787/2/147)
- Fox, A. J., Bordoloi, R., Savage, B. D., et al. 2015, *The Astrophysical Journal*, 799, L7, doi: [10.1088/2041-8205/799/1/17](https://doi.org/10.1088/2041-8205/799/1/17)
- Gehan, E. A. 1965, *Biometrika*, 52, 203. <http://www.jstor.org/stable/2333825>
- Gnat, O., & Sternberg, A. 2007, *The Astrophysical Journal Supplement Series*, 168, 213, doi: [10.1086/509786](https://doi.org/10.1086/509786)
- Grambsch, P. M., & Therneau, T. M. 1994, *Biometrika*, 81, 515, doi: [10.1093/biomet/81.3.515](https://doi.org/10.1093/biomet/81.3.515)
- Guo, F., & Mathews, W. G. 2012, *The Astrophysical Journal*, 756, 181, doi: [10.1088/0004-637x/756/2/181](https://doi.org/10.1088/0004-637x/756/2/181)
- Hanbury Brown, R., Davies, R. D., & Hazard, C. 1960, *The Observatory*, 80, 191
- Haslam, C. G. T., Salter, C. J., Stoffel, H., & Wilson, W. E. 1982, *A&AS*, 47, 1
- Karim, M. T., Fox, A. J., Jenkins, E. B., et al. 2018, *The Astrophysical Journal*, 860, 98, doi: [10.3847/1538-4357/aac167](https://doi.org/10.3847/1538-4357/aac167)
- Krishnarao, D., Benjamin, R. A., & Haffner, L. M. 2020, *The Astrophysical Journal*, 899, L11, doi: [10.3847/2041-8213/aba8f0](https://doi.org/10.3847/2041-8213/aba8f0)
- Lacki, B. C. 2014, *Monthly Notices of the Royal Astronomical Society*, 444, L39, doi: [10.1093/mnras/slu107](https://doi.org/10.1093/mnras/slu107)
- Lallement, R. 2022, *Comptes Rendus. Physique*, 23, S2, doi: [10.5802/crphys.97](https://doi.org/10.5802/crphys.97)
- LaRocca, D. M., Kaaret, P., Kuntz, K. D., et al. 2020, *The Astrophysical Journal*, 904, 54, doi: [10.3847/1538-4357/abbdff](https://doi.org/10.3847/1538-4357/abbdff)
- Lockman, F. J., Di Teodoro, E. M., & McClure-Griffiths, N. M. 2020, *The Astrophysical Journal*, 888, 51, doi: [10.3847/1538-4357/ab55d8](https://doi.org/10.3847/1538-4357/ab55d8)
- Magness, C. R., Fox, A., & Ashley, T. 2020, in *American Astronomical Society Meeting Abstracts*, Vol. 235, *American Astronomical Society Meeting Abstracts #235*, 205.03
- Mantel, N. 1966, *Cancer chemotherapy reports*, 50, 163. <http://europepmc.org/abstract/MED/5910392>
- McClure-Griffiths, N. M., Green, J. A., Hill, A. S., et al. 2013, *The Astrophysical Journal*, 770, L4, doi: [10.1088/2041-8205/770/1/14](https://doi.org/10.1088/2041-8205/770/1/14)
- Miller, R. G. J. 1981, *Survival Analysis* (New York: Wiley)
- Morton, D. C. 2003, *The Astrophysical Journal Supplement Series*, 149, 205, doi: [10.1086/377639](https://doi.org/10.1086/377639)

- Mou, G., Yuan, F., Bu, D., Sun, M., & Su, M. 2014, *The Astrophysical Journal*, 790, 109, doi: [10.1088/0004-637x/790/2/109](https://doi.org/10.1088/0004-637x/790/2/109)
- Mou, G., Sun, D., Fang, T., et al. 2023, *Nature Communications*, 14, 781, doi: [10.1038/s41467-023-36478-0](https://doi.org/10.1038/s41467-023-36478-0)
- Panopoulou, G. V., Dickinson, C., Readhead, A. C. S., Pearson, T. J., & Peel, M. W. 2021, *The Astrophysical Journal*, 922, 210, doi: [10.3847/1538-4357/ac273f](https://doi.org/10.3847/1538-4357/ac273f)
- Park, J.-W., Min, K.-W., Seon, K.-I., et al. 2007, *The Astrophysical Journal*, 665, L39, doi: [10.1086/521046](https://doi.org/10.1086/521046)
- Peto, R., & Peto, J. 1972, *Journal of the Royal Statistical Society. Series A (General)*, 135, 185. <http://www.jstor.org/stable/2344317>
- Planck Collaboration, Ade, P. A. R., Aghanim, N., et al. 2016, *A&A*, 594, A25, doi: [10.1051/0004-6361/201526803](https://doi.org/10.1051/0004-6361/201526803)
- Predehl, P., Sunyaev, R., & Becker, W. 2020, *Nature*, 588, 227. <https://doi.org/10.1038/s41586-020-2979-0>
- Qu, Z., & Bregman, J. N. 2019, *The Astrophysical Journal*, 880, 89, doi: [10.3847/1538-4357/ab2a0b](https://doi.org/10.3847/1538-4357/ab2a0b)
- Qu, Z., Bregman, J. N., Hodges-Kluck, E., Li, J.-T., & Lindley, R. 2020, *The Astrophysical Journal*, 894, 142, doi: [10.3847/1538-4357/ab774e](https://doi.org/10.3847/1538-4357/ab774e)
- R Core Team. 2023, *R: A Language and Environment for Statistical Computing*, R Foundation for Statistical Computing, Vienna, Austria. <https://www.R-project.org/>
- Remazeilles, M., Dickinson, C., Banday, A. J., Bigot-Sazy, M.-A., & Ghosh, T. 2015, *Monthly Notices of the Royal Astronomical Society*, 451, 4311, doi: [10.1093/mnras/stv1274](https://doi.org/10.1093/mnras/stv1274)
- Sarkar, K. C. 2018, *Monthly Notices of the Royal Astronomical Society*, 482, 4813, doi: [10.1093/mnras/sty2944](https://doi.org/10.1093/mnras/sty2944)
- Sarkar, K. C., Nath, B. B., & Sharma, P. 2015, *Monthly Notices of the Royal Astronomical Society*, 453, 3827, doi: [10.1093/mnras/stv1806](https://doi.org/10.1093/mnras/stv1806)
- Savage, B. D., Edgar, R. J., & Diplas, A. 1990, *ApJ*, 361, 107, doi: [10.1086/169172](https://doi.org/10.1086/169172)
- Savage, B. D., & Sembach, K. R. 1991, *The Astrophysical Journal*, 379, 245, doi: [10.1086/170498](https://doi.org/10.1086/170498)
- Savage, B. D., & Wakker, B. P. 2009, *The Astrophysical Journal*, 702, 1472, doi: [10.1088/0004-637x/702/2/1472](https://doi.org/10.1088/0004-637x/702/2/1472)
- Savage, B. D., Kim, T.-S., Fox, A. J., et al. 2017, *The Astrophysical Journal*, 232, 25, doi: [10.3847/1538-4365/aa8f4c](https://doi.org/10.3847/1538-4365/aa8f4c)
- Sofue, Y. 2015, *Monthly Notices of the Royal Astronomical Society*, 447, 3824, doi: [10.1093/mnras/stu2661](https://doi.org/10.1093/mnras/stu2661)
- . 2019, *Monthly Notices of the Royal Astronomical Society*, 484, 2954, doi: [10.1093/mnras/stz143](https://doi.org/10.1093/mnras/stz143)
- Sofue, Y., & Kataoka, J. 2021, *Monthly Notices of the Royal Astronomical Society*, 506, 2170, doi: [10.1093/mnras/stab1857](https://doi.org/10.1093/mnras/stab1857)
- Sofue, Y., & Reich, W. 1979, *A&AS*, 38, 251
- Su, M., Slatyer, T. R., & Finkbeiner, D. P. 2010, *The Astrophysical Journal*, 724, 1044, doi: [10.1088/0004-637x/724/2/1044](https://doi.org/10.1088/0004-637x/724/2/1044)
- Sun, X. H., Gaensler, B. M., Carretti, E., et al. 2013, *Monthly Notices of the Royal Astronomical Society*, 437, 2936, doi: [10.1093/mnras/stt2110](https://doi.org/10.1093/mnras/stt2110)
- Therneau, T. M. 2023, *A Package for Survival Analysis in R*. <https://CRAN.R-project.org/package=survival>
- Therneau, T. M., & Grambsch, P. M. 2000, *Modeling Survival Data: Extending the Cox Model* (New York: Springer)
- Wakker, B. P., Hernandez, A. K., French, D. M., et al. 2015, *The Astrophysical Journal*, 814, 40, doi: [10.1088/0004-637x/814/1/40](https://doi.org/10.1088/0004-637x/814/1/40)
- Wakker, B. P., Savage, B. D., Fox, A. J., Benjamin, R. A., & Shapiro, P. R. 2012, *The Astrophysical Journal*, 749, 157, doi: [10.1088/0004-637X/749/2/157](https://doi.org/10.1088/0004-637X/749/2/157)
- Yang, H.-Y. K., Ruszkowski, M., Ricker, P. M., Zweibel, E., & Lee, D. 2012, *The Astrophysical Journal*, 761, 185, doi: [10.1088/0004-637x/761/2/185](https://doi.org/10.1088/0004-637x/761/2/185)
- Yang, H. Y. K., Ruszkowski, M., & Zweibel, E. G. 2022, *Nature Astronomy*, 6, 584, doi: [10.1038/s41550-022-01618-x](https://doi.org/10.1038/s41550-022-01618-x)
- Yusef-Zadeh, F., Hewitt, J. W., Arendt, R. G., et al. 2009, *The Astrophysical Journal*, 702, 178, doi: [10.1088/0004-637x/702/1/178](https://doi.org/10.1088/0004-637x/702/1/178)
- Zheng, Y., Peek, J. E. G., Putman, M. E., & Werk, J. K. 2019, *The Astrophysical Journal*, 871, 35, doi: [10.3847/1538-4357/aaf6eb](https://doi.org/10.3847/1538-4357/aaf6eb)
- Zubovas, K., King, A. R., & Nayakshin, S. 2011, *Monthly Notices of the Royal Astronomical Society*, 415, L21, doi: [10.1111/j.1745-3933.2011.01070.x](https://doi.org/10.1111/j.1745-3933.2011.01070.x)

APPENDIX

A. SAMPLE LIV Si IV MEASUREMENTS

We list basic information on the GC sample use for this study in Table A1. We also list the $\log(N_a)$ for the LIV Si IV $\lambda\lambda$ 1393, 1402, the adopted Si IV $\log(N_a)$, and the $N_{a,R}$ measurements.

Table A1. LIV Si IV Measurements in COS AGN sight lines in the Galactic Center Region

| Sight Line | l ($^\circ$) | b ($^\circ$) | Location | $\log N_{a,1393}^a$ | $\log N_{a,1402}^b$ | $\log N_{a,\text{adop.}}^c$ | $N_{a,R}^d$ | PID ^e | Ref. ^f |
|-------------------------|------------------|------------------|--------------|-------------------------|-----------------------|-----------------------------|----------------------------|------------------|-------------------|
| RXJ1342.7+1844 | 0.24 | 75.52 | eB, LNPS | $\geq 13.70 \pm 0.03$ | $\geq 13.88 \pm 0.04$ | ≥ 13.88 | $\geq 3.1 \times 10^{13}$ | 12248 | 2 |
| HE2332-3556 | 0.59 | -71.59 | eB | 13.31 ± 0.06 | 13.44 ± 0.09 | 13.38 ± 0.12 | -1.2×10^{13} | 13444 | 3 |
| RBS2023 | 0.61 | -71.62 | eB | 13.40 ± 0.04 | ND ^g | 13.40 ± 0.04 | -1.1×10^{13} | 13444 | 3 |
| SDSSJ151237.15+012846.0 | 1.80 | 47.50 | FB, eB | $\geq 13.98 \pm 0.03$ | $\geq 14.07 \pm 0.05$ | ≥ 14.07 | $\geq 5.3 \times 10^{13}$ | 12603 | 2 |
| MRK1392 | 2.80 | 50.30 | FB, eB, LNPS | $\geq 13.68 \pm 0.01$ | 13.77 ± 0.02 | ≥ 13.77 | $\geq -2.2 \times 10^{12}$ | 13448 | 2 |
| SDSSJ135712.60+170444.0 | 2.90 | 71.80 | eB, LNPS | $\leq 13.80 \pm 0.01^h$ | 13.79 ± 0.02 | 13.79 ± 0.02 | 1.6×10^{13} | 12248 | 2 |
| 1H1613-097 | 3.50 | 28.50 | FB, eB | $\geq 13.76 \pm 0.02$ | 13.84 ± 0.03 | 13.84 ± 0.03 | -3.4×10^{13} | 13448 | 2 |
| PG1352+183 | 4.40 | 72.90 | eB, LNPS | 13.68 ± 0.01 | 13.69 ± 0.02 | 13.69 ± 0.02 | 2.4×10^{12} | 13448 | 2 |
| RBS1768 | 4.51 | -48.46 | FB, eB | 13.59 ± 0.02 | 13.58 ± 0.03 | 13.59 ± 0.04 | -1.5×10^{12} | 12936 | 3 |
| CTS487 | 5.54 | -69.44 | eB | 13.36 ± 0.03 | 13.32 ± 0.07 | 13.34 ± 0.07 | -1.4×10^{13} | 13448 | 3 |
| RBS1454 | 5.60 | 52.90 | FB, eB, LNPS | ... ^h | $\geq 13.95 \pm 0.03$ | ≥ 13.95 | $\geq 3.1 \times 10^{13}$ | 12603 | 2 |
| SDSSJ150928.30+070235.0 | 7.80 | 51.60 | FB, eB, LNPS | $\geq 13.85 \pm 0.02^i$ | $\geq 13.79 \pm 0.05$ | ≥ 13.79 | $\geq 2.4 \times 10^{12}$ | 12603 | 2 |
| UVQSJ191928.05-295808.0 | 8.18 | -18.77 | FB, eB | ... ^h | 13.97 ± 0.01 | 13.97 ± 0.01 | 4.3×10^{11} | 15339 | 4 |
| SDSSJ141542.90+163413.7 | 8.80 | 67.80 | eB, LNPS | $\geq 13.85 \pm 0.01$ | 13.90 ± 0.02 | 13.90 ± 0.02 | 3.2×10^{13} | 12486 | 2 |
| SDSSJ151507.43+065708.3 | 9.00 | 50.40 | FB, eB, LNPS | $\geq 13.93 \pm 0.03$ | $\geq 13.99 \pm 0.04$ | ≥ 13.99 | $\geq 3.8 \times 10^{13}$ | 12603 | 2 |
| PDS456 | 10.40 | 11.20 | FB, eB | $\geq 14.05 \pm 0.01$ | 14.02 ± 0.02 | 14.02 ± 0.02 | -7.6×10^{13} | 13448 | 1,2 |
| MRK841 | 11.20 | 54.60 | eB, LNPS | $\geq 13.91 \pm 0.01$ | 14.05 ± 0.01 | ≥ 14.05 | $\geq 5.7 \times 10^{13}$ | 13448 | 2 |
| ESO462-G09 | 11.33 | -31.95 | FB, eB | $\geq 13.62 \pm 0.03$ | 13.61 ± 0.07 | 13.61 ± 0.07 | -1.6×10^{13} | 13448 | 3 |
| RBS2070 | 12.84 | -78.04 | eB | 13.33 ± 0.04 | 13.40 ± 0.07 | 13.37 ± 0.08 | -1.3×10^{13} | 12864 | 3 |
| SDSSJ150952.19+111047.0 | 13.60 | 53.80 | eB, LNPS | $\geq 13.79 \pm 0.02$ | $\geq 14.18 \pm 0.02$ | ≥ 14.18 | $\geq 9.6 \times 10^{13}$ | 12614 | 2 |
| PG1522+101 | 14.90 | 50.10 | FB, eB, LNPS | ... ^h | 13.70 ± 0.02 | 13.70 ± 0.02 | -8.0×10^{12} | 11741 | 2 |
| PKS2155-304 | 17.73 | -52.25 | eB | 13.36 ± 0.02 | 13.35 ± 0.03 | 13.36 ± 0.04 | -1.4×10^{13} | 8125/12038 | 3 |
| SDSSJ154553.48+093620.5 | 18.30 | 45.40 | FB, eB, LNPS | $\geq 13.98 \pm 0.02$ | ... ^h | ≥ 13.98 | $\geq 3.3 \times 10^{13}$ | 12248 | 2 |
| UVQSJ192636.95-182553.0 | 20.00 | -15.86 | eB | $\geq 14.14 \pm 0.01$ | $\geq 14.14 \pm 0.01$ | ≥ 14.14 | $\geq 4.5 \times 10^{13}$ | 15339 | 4 |
| RXJ1303.7+2633 | 21.80 | 87.20 | - | $\geq 13.90 \pm 0.03$ | ... ^h | ≥ 13.90 | $\geq 3.7 \times 10^{13}$ | 13382 | 2 |
| PG1553+113 | 21.90 | 44.00 | FB, eB, LNPS | ... ^h | 13.91 ± 0.01 | 13.91 ± 0.01 | 1.9×10^{13} | 11520/12025 | 2 |
| SDSSJ141038.39+230447.1 | 24.60 | 71.60 | eB | ... ^h | ... ^h | ... | ... | 12958 | 2 |
| SDSSJ135424.90+243006.3 | 25.90 | 75.60 | - | $\geq 13.68 \pm 0.04$ | ... ^h | ≥ 13.68 | $\geq 3.5 \times 10^{12}$ | 12603 | 2 |
| SDSSJ134822.31+245650.1 | 26.40 | 77.00 | - | $\geq 14.00 \pm 0.03$ | $\geq 14.09 \pm 0.05$ | ≥ 14.09 | $\geq 7.9 \times 10^{13}$ | 12603 | 2 |
| RXJ1605.3+1448 | 27.80 | 43.40 | eB, LNPS | $\geq 13.82 \pm 0.01$ | ... ^h | ≥ 13.82 | $\geq 6.8 \times 10^{12}$ | 12614 | 2 |
| SDSSJ131802.01+262830.3 | 28.20 | 84.00 | - | ... ^h | $\geq 13.53 \pm 0.15$ | ≥ 13.53 | $\geq -9.0 \times 10^{12}$ | 12603 | 2 |
| RXJ1356.4+2515 | 29.30 | 75.30 | - | $\geq 13.83 \pm 0.02$ | $\geq 13.91 \pm 0.02$ | ≥ 13.91 | $\geq 3.7 \times 10^{13}$ | 12248 | 2 |
| PG1424+240 | 29.50 | 68.20 | eB, LNPS | ... ^h | 13.68 ± 0.03 | 13.68 ± 0.03 | 2.3×10^{12} | 12612 | 2 |
| NGC5548 | 32.00 | 70.50 | - | $\geq 13.77 \pm 0.01$ | 13.83 ± 0.01 | ≥ 13.83 | $\geq 2.3 \times 10^{13}$ | 7572 | 2 |
| MRK877 | 32.90 | 41.10 | eB, LNPS | 13.84 ± 0.01 | 13.87 ± 0.02 | 13.86 ± 0.02 | 1.2×10^{13} | 12569 | 2 |
| 3C323.1 | 33.90 | 49.50 | eB, LNPS | $\geq 13.83 \pm 0.01$ | 13.85 ± 0.03 | 13.85 ± 0.03 | 1.9×10^{13} | 13398 | 2 |
| QSO1503-4152 | 327.70 | 14.60 | eB | $\geq 13.91 \pm 0.01$ | $\geq 14.01 \pm 0.03$ | ≥ 14.01 | $\geq -1.1 \times 10^{13}$ | 11659 | 2 |
| HE1340-0038 | 328.80 | 59.40 | eB | 13.46 ± 0.05 | 13.69 ± 0.06 | 13.59 ± 0.08 | -9.3×10^{12} | 11598/13033 | 2 |

Table A1 continued

Table A1 (*continued*)

| Sight Line | l ($^\circ$) | b ($^\circ$) | Location | $\log N_{a,1393}^a$ | $\log N_{a,1402}^b$ | $\log N_{a,\text{adop.}}^c$ | $N_{a,R}^d$ | PID ^e | Ref. ^f |
|-------------------------|------------------|------------------|----------|-------------------------|-----------------------|-----------------------------|----------------------------|------------------|-------------------|
| SDSSJ131545.21+152556.3 | 329.90 | 77.00 | eB, LNPS | ... ^h | $\geq 13.66 \pm 0.08$ | ≥ 13.66 | $\geq 1.7 \times 10^{12}$ | 12603 | 2 |
| HE2259-5524 | 330.64 | -55.72 | eB | 13.51 ± 0.03^i | 13.42 ± 0.07^i | 13.47 ± 0.07 | -5.8×10^{12} | 13444 | 3 |
| HE2258-5524 | 330.72 | -55.67 | eB | 13.36 ± 0.03^i | 13.41 ± 0.05^i | 13.39 ± 0.06 | -1.1×10^{13} | 13444 | 3 |
| IRASF21325-6237 | 331.14 | -45.52 | eB | 13.64 ± 0.01 | 13.67 ± 0.02 | 13.66 ± 0.02 | 7.1×10^{12} | 12936 | 3 |
| RXJ1342.1+0505 | 333.90 | 64.90 | eB | $\geq 13.58 \pm 0.04$ | 13.62 ± 0.07 | 13.62 ± 0.07 | -5.4×10^{12} | 12248 | 2 |
| SDSSJ125846.66+242739.1 | 335.10 | 86.90 | - | $\geq 13.65 \pm 0.03$ | ... ^h | ≥ 13.65 | $\geq 2.2 \times 10^{12}$ | 13382 | 2 |
| ESO141-G55 | 338.18 | -26.71 | FB, eB | 13.79 ± 0.01 | 13.78 ± 0.01 | 13.79 ± 0.01 | 1.5×10^{12} | 12936 | 3 |
| RBS1897 | 338.51 | -56.63 | eB | $\geq 13.30 \pm 0.02$ | 13.42 ± 0.03 | ≥ 13.42 | $\geq -9.4 \times 10^{12}$ | 11686 | 3 |
| SDSSJ135726.27+043541.4 | 340.80 | 62.50 | eB | ... ^h | $\geq 13.97 \pm 0.02$ | ≥ 13.97 | $\geq 4.4 \times 10^{13}$ | 12264 | 2 |
| UVQSJ185649.37-544229.9 | 341.66 | -22.60 | FB, eB | $\geq 13.88 \pm 0.02$ | $\geq 13.89 \pm 0.04$ | ≥ 13.89 | $\geq 5.5 \times 10^{12}$ | 15339 | 4 |
| SDSSJ140655.66+015712.8 | 341.80 | 59.00 | eB | ... ^h | $\geq 13.64 \pm 0.10$ | ≥ 13.64 | $\geq -7.2 \times 10^{12}$ | 12603 | 2 |
| PG1435-067 | 344.00 | 47.20 | FB, eB | 13.57 ± 0.02 | 13.61 ± 0.04 | 13.59 ± 0.05 | -2.3×10^{13} | 12569/13448 | 2 |
| RBS1892 | 345.90 | -58.37 | eB | 13.48 ± 0.02^i | 13.53 ± 0.04^i | 13.51 ± 0.05 | -4.0×10^{12} | 12604 | 3 |
| SDSSJ142614.79+004159.4 | 347.60 | 55.10 | eB | $\geq 13.96 \pm 0.03$ | $\geq 13.97 \pm 0.04$ | ≥ 13.97 | $\geq 3.9 \times 10^{13}$ | 13473 | 2 |
| RBS2000 | 350.20 | -67.58 | eB | 13.55 ± 0.02 | 13.61 ± 0.04 | 13.58 ± 0.05 | 2.4×10^{12} | 13448 | 3 |
| PKS2005-489 | 350.37 | -32.60 | FB, eB | $\geq 13.97 \pm 0.01$ | 14.02 ± 0.01 | ≥ 14.02 | $\geq 4.9 \times 10^{13}$ | 11520 | 3 |
| RXJ1429.6+0321 | 351.80 | 56.60 | eB | $\geq 13.77 \pm 0.04$ | $\geq 13.84 \pm 0.06$ | ≥ 13.84 | $\geq 1.5 \times 10^{13}$ | 12603 | 2 |
| SDSSJ141949.39+060654.0 | 351.90 | 60.30 | eB | $\geq 13.78 \pm 0.03$ | ... ^h | ≥ 13.78 | $\geq 8.7 \times 10^{12}$ | 13473 | 2 |
| UVQSJ185302.65-415839.6 | 354.36 | -18.04 | FB, eB | $\geq 14.03 \pm 0.01$ | 13.92 ± 0.02 | ≥ 13.92 | $\geq -1.7 \times 10^{13}$ | 15339 | 4 |
| RBS1795 | 355.18 | -50.86 | FB, eB | $\geq 13.54 \pm 0.01$ | 13.70 ± 0.02 | ≥ 13.70 | $\geq 1.1 \times 10^{13}$ | 11541 | 3 |
| UVQSJ193819.59-432646.3 | 355.47 | -26.41 | FB, eB | $\geq 13.86 \pm 0.03^h$ | 13.87 ± 0.02^h | 13.87 ± 0.02 | 3.8×10^{12} | 15339 | 4 |
| HS1302+2510 | 357.40 | 86.30 | - | $\geq 13.74 \pm 0.02$ | 13.69 ± 0.06 | 13.69 ± 0.06 | 6.4×10^{12} | 13382 | 2 |
| RBS1666 | 335.73 | -31.00 | FB, eB | $\geq 13.89 \pm 0.01$ | 13.89 ± 0.02 | 13.89 ± 0.02 | 2.5×10^{13} | 13448 | 3 |

^aThe log of the apparent column density (N_a in cm^{-2}) measured from Si IV $\lambda 1393$ absorption in the range $-100 < v_{\text{LSR}} < 100 \text{ km s}^{-1}$.

^bThe log of the apparent column density (N_a in cm^{-2}) measured from Si IV $\lambda 1402$ absorption in the range $-100 < v_{\text{LSR}} < 100 \text{ km s}^{-1}$.

^cThe adopted log apparent column density used for statistical analysis. See Section 2 for a discussion on how $\log N_{a,\text{adop.}}$ was calculated.

^dThe residual apparent column density used for statistical analysis. See Section 3.2 for a discussion on how $N_{a,R}$ was calculated.

^eHubble Space Telescope Proposal ID number.

^fReferences: (1) Fox et al. (2015) (2) Bordoloi et al. (2017) (3) Karim et al. (2018) (4) Ashley et al. (2020).

^gND = not detected.

^hThese measurements are affected by interfering emission (e.g. Lyman- α or intergalactic absorption) and were therefore set as an upper limit. If the line was saturated and affected by interfering absorption, then the line could not be measured and ‘...’ was placed in the measurement.

ⁱHVC absorption identified in the associated reference is likely contributing to the LIV absorption in the $|v_{\text{LSR}}| < 100 \text{ km s}^{-1}$.

B. SURVIVAL ANALYSIS

In Figure B1 we show two examples of survival curves created using `survfit` for the model-subtracted residual analysis. The plots start on the y-axis at 100% ‘survival’ and drop by the percent of sight lines with an unsaturated detection at the specified column density on the x-axis. The `survdif` function determines if these two curves are drawn from different populations.

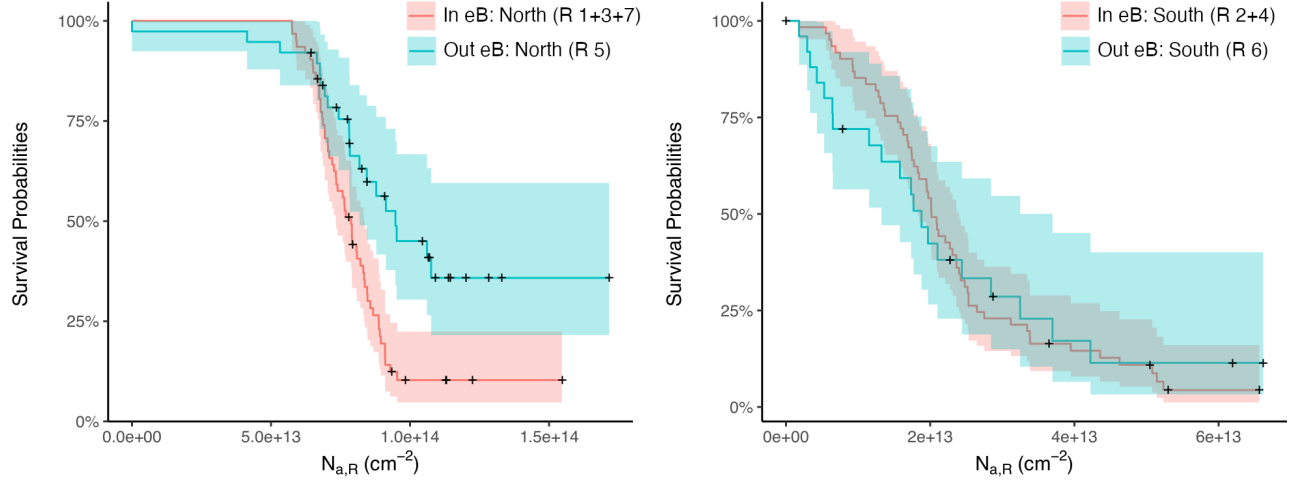


Figure B1. Two examples of survival curves used in the analysis in Section 3.2. The residual columns displayed on the x-axes are offset by the minimum residuals for each pair of spatially compared groups, -7.6×10^{13} and -1.7×10^{13} for the left and right plots, respectively, in order to obtain only positive numbers for the analysis. In both plots the shaded regions denote the 95% confidence levels. Left: An example of different populations: inside the northern eB vs. outside the eB in the northern hemisphere. Right: An example of populations that were not shown to be different: inside the southern eB vs. outside the eB in the southern hemisphere.